ACS OMEGA

http://pubs.acs.org/journal/acsodf

Article

Comparative Analysis of Four Neural Network Models on the Estimation of CO_2−Brine Interfacial Tension

Xiaojie Liu, Meiheriayi Mutailipu, Jiafei Zhao, and Yu Liu*

Cite This: *ACS Omega* 2021, 6, 4282−4288

Read Online

ACCESS | Metrics & More | Article Recommendations

ABSTRACT: During the CO_2 injection of geological carbon sequestration and CO_2-enhanced oil recovery, the contact of CO_2 with underground salt water is inevitable, where the interfacial tension (IFT) between gas and liquid determines whether the projects can proceed smoothly. In this paper, three traditional neural network models, the wavelet neural network (WNN) model, the back propagation (BP) model, and the radical basis function model, were applied to predict the IFT between CO_2 and brine with temperature, pressure, monovalent cation molality, divalent cation molality, and molar fraction of methane and nitrogen impurities. A total of 974 sets of experimental data were divided into two data groups, the training group and the testing group. By optimizing the WNN model (I_WNN), a most stable and precise model is established, and it is found that temperature and pressure are the main parameters affecting the IFT. Through the comparison of models, it is found that I_WNN and BP models are more suitable for the IFT evaluation between CO_2 and brine.

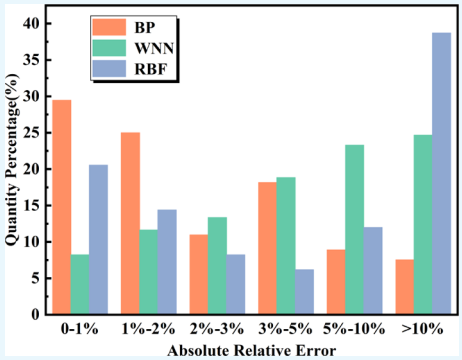

1. INTRODUCTION

The CO_2 content in the atmosphere is increasing year by year. According to the latest report released by the International Energy Agency[1] in March 2019, the global energy-related carbon dioxide emissions increased by 1.7% compared with last year, reaching 3.31 billion tons, and it is at a record high. The greenhouse effect caused by high CO_2 content has become an urgent problem to be solved. In order to combat climate change, researchers have found that CO_2 can be injected into gas reservoirs, coal seams that cannot be exploited, and deep saline alkali aquifers, or CO_2-enhanced oil displacement can be used to store CO_2 in the reservoir,[2] so as to reduce the CO_2 content in the atmosphere. On the other hand, the interface property between CO_2 and liquid is the key to control multiple flow behaviors in the CO_2 geological storage process.[3] The interfacial tension (IFT) of CO_2 and brine determines whether CO_2 can break through capillary force and damage reservoir safety.[4] Therefore, it is very important to know exactly the CO_2−brine IFT in underground CO_2 storage.

The IFT is mainly obtained by experimental methods, empirical formula methods, and some theoretical model methods. At present, there are a large number of experimental CO_2−brine IFT data provided by researchers.[5−19] These experiments are mainly carried out by using the pendant drop method, covering a wide range of temperature and pressure, comprehensively considering other variables that may cause IFT changes, including cations (K^+, Ca^{2+}, Na^+, Mg^{2+}, etc.) in liquid and components of surrounding gas environment (nitrogen, methane, and carbon dioxide). However, the experimental method is usually time- and labor-consuming, and the experimental apparatus costs a lot of money. The theoretical methods,[20−31] including molecular dynamics simulation and theoretical calculation, give theoretical guidance for understanding the influence of temperature, pressure, salinity, and the gas environment on IFT. The molecular dynamics simulation method can observe the microcosmic characteristics of the two-phase interface more intuitively, and theoretical calculation is convenient to evaluate the influence degree of variable parameters. However, because of the huge amount of theoretical calculation, it is necessary to be proficient in molecular characteristics. The method is easy to lead to the difference of results between different groups in terms of temperature, and the prediction results are too high under high-pressure conditions. The molecular dynamics simulation method needs to be carried out under ideal conditions, and therefore, the application is limited.

Many researchers try to find a reliable and convenient method to predict the IFT under various conditions. Zhang et al.[4] summarized the prediction models of Hebach et al.,[14] Chalbaud et al.,[11] and Li et al.[15,17] and evaluated the

Received: October 29, 2020
Accepted: December 29, 2020
Published: February 2, 2021

https://dx.doi.org/10.1021/acsomega.0c05290
ACS Omega 2021, 6, 4282−4288

performance of pure CO_2−water and pure/impure CO_2−brine from the mean absolute error (MAE), mean absolute relative error (MARE), mean squared error (MSE), and determination coefficient (R^2), although Li et al.'s[17] model ranks the highest among these methods, but when the IFT is greater than 60 mN/m, the model fails to guaranty its accuracy of prediction. Then, Zhang summarized up to 1716 data points and proposed an artificial neural network (ANN) model with the topology 6-10-20-1, which obtained prediction results well.

Yasser et al.[32] reviewed the application of square gradient theory, linear gradient theory, density functional theory, drop shape analysis, axisymmetric drop-shape analysis, density gradient theory, and other methods for the prediction of IFT. They collected 576 data sets and established water-based binary and ternary (CO_2, CH_4, and N_2) IFT models under elevated pressure by using neuroevolutionary technology. The MAE and R^2 of the predicted data of the model are 3.34% and 0.999, respectively, which are compared with the relevant literatures,[4,11,14,15,17,33] and highest accuracy was achieved. However, these models are not suitable for complex environments because of their few parameters.

In recent years, Niroomand-Toomaj et al.,[34] Partovi et al.,[35] and Chen and Yang[36] have adopted a multilayer perceptron model, least squares support vector machine, adaptive neurofuzzy inference system, radial basis function network optimized by particle swarm optimization method, adaptive neurofuzzy inference system trained by a hybrid method, and mutual solubility model; the models are established for temperature, pressure, salinity/molality concentration, and gas mole fraction, all of which have achieved high prediction accuracy.

This work aims to establish the IFT model of temperature and pressure, mass molality concentration of monovalent cation, mass molality concentration of divalent cation, methane and nitrogen fraction from the existing IFT database, and to analyze the prediction effect of wavelet neural network (WNN), back propagation (BP), and radical basis function (RBF) neural network model in predicting IFT of CO_2−brine. By optimizing the WNN model and comparing the BP model, the reasons for the differences were analyzed, and the advantages and disadvantages of various network models and their applicability to specific situations were compared.

2. BASICS OF MODELS

By simulating the information processing mode between brain neurons, the ANN conducts parallel processing and nonlinear transformation of information to establish the relationship between input data and output data. The schematic diagram of the neural network is shown in Figure 1. The performance of the ANN is mainly determined by the topological structure, excitation function, learning rules, and sample quality. The BP, WNN, and RBF model achieve different prediction effects by changing one or two performance conditions.

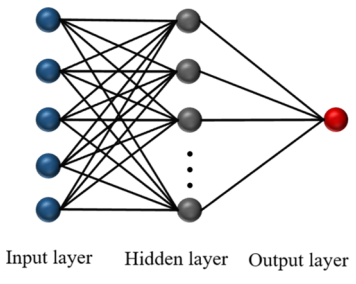

Figure 1. ANN structure.

2.1. BP Model. The BP neural network is a kind of multilayer forward feedback neural network, and the BP algorithm is used to adjust the network weight. The core of the BP algorithm is the theory of negative gradient descent, that is, the error adjustment direction is always along the direction with the fastest descent.

For the n-layer network, the initial weight $w_{ij}(0)$ and threshold $B_{ij}(0)$ between each layer of the network are given a $[-1,1]$ random matrix, $i = 1...n - 1$, $j = i + 1$.

The input and output of the first layer are I_1 and O_1, $I_1 = O_1 = X$, and X is the input data. The input and output of j-th are $I_j = W_{ij} \times O_i + B_{ij} \times \text{ones}$, $O_j = F(I_j)(I_j)$.

The activation function $f^{(ij)}$ used between the input layer, the hidden layer, and the output layer is usually different, and generally are of the following two types

① The sigmoid function

$$f^{(ij)} = \frac{1 - e^{-I_j}}{1 + e^{-I_j}} \tag{1}$$

② Linear function

$$f^{(ij)} = I_j \tag{2}$$

Energy error function

$$E = \sum (Y - O_n)^2 \tag{3}$$

where Y is the actual output and E is the total error value.

The weight and threshold learning function of gradient descent driven by quantity is adjusted by the momentum gradient descent method.[37] For $t + 1$, the following relation is satisfied

$$w_{ij}(t + 1) = -\eta \frac{\partial E}{\partial w_{ij}} + w_{ij}(t) = \Delta w_{ij} + w_{ij}(t) \tag{4}$$

$$B_{ij}(t + 1) = -\eta \frac{\partial E}{\partial B_{ij}} + B_{ij}(t) = \Delta B_{ij} + B_{ij}(t) \tag{5}$$

where η is the learning rate, $\eta \in [0,1]$.

2.2. WNN Model. A wavelet is a waveform with a finite length and an average of 0. The difference between the wavelet network and BP network is that the activation function of the wavelet network is the wavelet basis function. The definition of the wavelet basis function can be seen in ref38 Thus, the hidden layer output

$$H = f\left(\frac{\sum w_{ij}X - b}{a}\right) \tag{6}$$

a is the expansion factor, and b is the translation factor.

In this paper, wavelet basis function f is selected as Morlet function

$$y = \cos(1.75x)e^{-x^2/2} \tag{7}$$

WNN uses the wavelet function as the node activation function. The neural network combines the time-frequency localization function of the wavelet transform and the self-learning function of the neural network to solve the problem of poor convergence and divergence.

https://dx.doi.org/10.1021/acsomega.0c05290
ACS Omega 2021, 6, 4282−4288

Table 1. Ranges of CO_2−Brine IFT Used in the Models

	pressure (MPa)	temperature (°C)	monovalent cation molality (mol/kg)	divalent cation molality (mol/kg)	CH_4 (mol %)	N_2 (mol %)	measured IFT (mN/m)
max	175	60.05	2.75	2.7	100	100	74
min	5.25	0.1	0	0	0	0	16.1

2.3. RBF Model. The network structure of RBF has three layers. The activation functions of the first layer and the third layer are linear functions. The Gaussian function used in the hidden layer is as follows

$$\boldsymbol{R}(x) = e^{-\|\boldsymbol{x}-\boldsymbol{c}\|^2/2\sigma^2} \tag{8}$$

where $\mathbf{x} = (x_1, x_2, x_3, ..., x_j)^T$, j is the number of input variables, $\mathbf{c}$ denotes the center vector, and σ is the radius or width of the hidden neuron.

3. DATA ACQUISITION

The IFT between CO_2 and brine is affected by many factors. In summary of previous experiments,[5,6,8,10−16,18,19] the independent variables commonly used in IFT between CO_2 and brines are temperature, pressure, molality (Na^+, K^+, Ca^{2+}, Mg^{2+}), molar fraction (CH_4, N_2), and density difference, all of which cover all the variables that affect the changes of IFT.

A total of 974 data sets[5,6,16] measured by the suspension drop method were collected in this paper, including a pure/impure CO_2 gas environment, impure gas containing CH_4 and N_2, salt water solutes such as NaCl, KCl, $CaCl_2$, and $MgCl_2$. The data range is shown in Table 1. Studies in literature[15,16] measured the changes in IFT between CO_2 and brine containing Na^+, K^+, Ca^{2+}, and Mg^{2+}; according to the experimental results, cations with identical valency obtained in the same environment had similar effect on CO_2−brine IFT, so cations with identical valency were taken as the same variable.

4. MODEL DEVELOPMENT

In order to establish a reliable model to characterize the CO_2−brine IFT and evaluate its prediction effect, the input variables include temperature T (°C), pressure P (MPa), molality of monovalent cation m_1 (mol/kg), molality of divalent cation m_2 (mol/kg), and mole fraction of CH_4 and N_2 (%). The following functional relationships can be summarized

$$\text{IFT} = f(P, T, m_1, m_2), C(CH_4), C(N_2) \tag{9}$$

First, the target and result in the input data are normalized to make the distribution between $[-1,1]$

$$I = \frac{2(I_n - I_{\min})}{(I_{\max} - I_{\min})} - 1 \tag{10}$$

Then, the collected database was randomly divided into the training set (70%) and testing set (30%). The BP, WNN, and RBF were used to establish the models and test the prediction ability. For BP and WNN models, 15 neurons are used in the hidden layer, which was the number of best prediction results for both BP and WNN models obtained by the trial and error method. In order to determine the influence of the activation function, the initial transfer vector of the WNN model is optimized as follows: 1000 transfer vectors are randomly generated, each vector carries out 200 iterations, and the transfer vector with the smallest energy error value is selected as the optimal transfer vector. Take this vector as the initial transfer vector to calculate the predicted value and final prediction error of the WNN model. The RBF model uses the newrb function of the MATLAB toolkit. The hidden layer increases by 25 neurons at a time; the final number of neurons adopts the default value, that is, the number equal to the number of training sets. The data width increases by 0.1 each time from 0.2 to 0.7; it is found that 0.5 data width can get the highest accuracy.

5. RESULTS AND DISCUSSION

5.1. Result Processing. Different norms are used to evaluate the data results. Currently, norms commonly used in literature[4,39] include MAE, MARE, MSE, and R^2. (mea means measured IFT, est means estimated IFT)

$$\text{MAE} = \frac{1}{N}\sum_{i=1}^{N} |y_i^{\text{est}} - y_i^{\text{mea}}| \tag{11}$$

$$\text{MARE} = \frac{1}{N}\sum_{i=1}^{N}\left(\frac{|y_i^{\text{est}} - y_i^{\text{mea}}|}{y_i^{\text{mea}}}\right) \times 100 \tag{12}$$

$$\text{MSE} = \frac{1}{N}\sum_{i=1}^{N} (y_i^{\text{est}} - y_i^{\text{mea}})^2 \tag{13}$$

$$R^2 = 1 - \frac{\sum (y_i^{\text{mea}} - y_i^{\text{est}})^2}{\sum (y_i^{\text{mea}} - \overline{y_i^{\text{mea}}})^2} \tag{14}$$

The following norms are provided for further verification.[39]

$$k = \frac{\sum y_i^{\text{mea}} y_i^{\text{est}}}{\sum (y_i^{\text{est}})^2} \tag{15}$$

$$k' = \frac{\sum y_i^{\text{mea}} y_i^{\text{est}}}{\sum (y_i^{\text{mea}})^2} \tag{16}$$

$$0.85 \le k \le 1.15 \tag{17}$$

$$0.85 \le k' \le 1.15 \tag{18}$$

$$R_o^2 = 1 - \frac{\sum (y_i^{\text{est}} - k y_i^{\text{est}})^2}{\sum (y_i^{\text{est}} - \overline{y^{\text{est}}})^2} \tag{19}$$

$$R_o'^2 = 1 - \frac{\sum (y_i^{\text{mea}} - k y_i^{\text{mea}})^2}{\sum (y_i^{\text{mea}} - \overline{y_i^{\text{mea}}})^2} \tag{20}$$

$$m = \frac{R^2 - R_o^2}{R^2} \le 0.1 \tag{21}$$

$$n = \frac{R^2 - R_o'^2}{R^2} \le 0.1 \tag{22}$$

$$R_m^2 = R^2 \times (1 - \sqrt{|R^2 - R_o^2|}) \ge 0.5 \tag{23}$$

https://dx.doi.org/10.1021/acsomega.0c05290
ACS Omega 2021, 6, 4282−4288

Table 2. Different Norms Computed to Assess the BP, WNN, and RBF Models for Predicting CO_2−Brine IFT

	all			training set			testing set		
	BP	WNN	RBF	BP	WNN	RBF	BP	WNN	RBF
MAE	1.1557	2.6642	6.8018	1.1088	2.5956	0.4213	1.2652	2.8242	22.0167
MARE	3.2020	7.4214	17.3754	3.1115	7.2569	1.2546	3.4133	7.8057	55.8174
MSE	3.4115	13.2312	1709.1726	3.2375	12.5932	1.2357	3.8178	14.7214	5781.9453
R^2	0.9797	0.9211	−9.2015	0.9811	0.9263	0.9928	0.9761	0.9080	−35.2507
k	1.0013	1.0170	0.5427	1.0007	1.0140	1.0001	1.0028	1.0241	0.2647
k'	0.9970	0.9771	1.0108	0.9977	0.9802	0.9993	0.9954	0.9698	1.0382
R_o^2	1.0000	0.9965	0.5829	1.0000	0.9977	1.0000	0.9999	0.9924	0.2841
$R_o'^2$	0.9999	0.9937	0.9986	0.9999	0.9954	1.0000	0.9997	0.9886	0.9814
m	−0.0207	−0.0819	1.0633	−0.0193	−0.0771	−0.0073	−0.0243	−0.0930	1.0081
n	−0.0207	−0.0788	1.1085	−0.0192	−0.0745	−0.0073	−0.0242	−0.0887	1.0278
R_m^2	0.8400	0.6681	19.5808	0.8461	0.6788	0.9084	0.8257	0.6442	174.8824

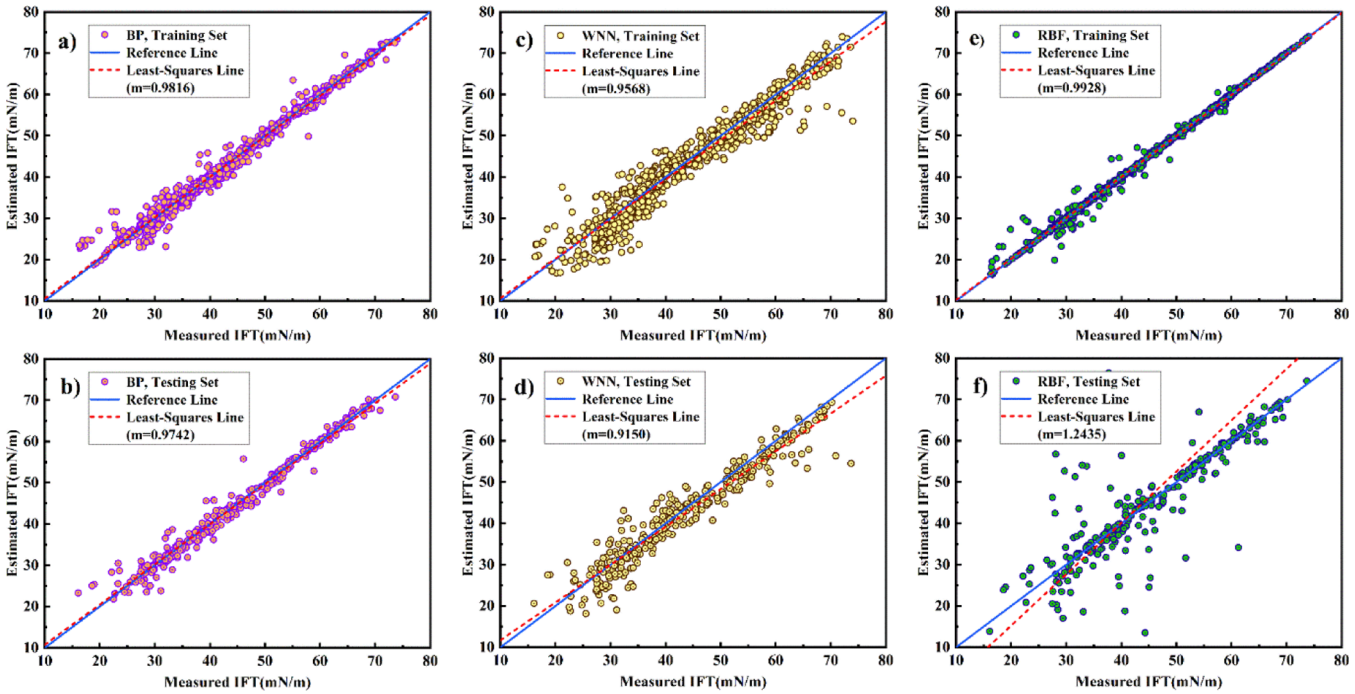

Figure 2. Comparison between the results obtained by the models studied (i.e. BP, WNN, and RBF) in current research and the actual data of CO_2−brine IFT. (m is the slope of the least-squares line).

The WNN, BP, and RBF methods about the norms of the calculation results are shown in Table 2; the unreliable estimated data sets of the RBF model are deleted (too high or too low). Because the initial transfer vector is randomly generated, the results of WNN and BP methods will change with the change of the initial transfer vector; this paper lists the WNN and BP methods' single run results. The operation result will not change when the initial parameters of RBF methods are determined. It can be seen from Table 2 that all the parts of BP and WNN and all the parameters in the training set of RBF meet the above criteria, indicating that these prediction methods are reliable and effective. In addition, regardless of whether in the training set or in the test set, it can be seen from various parameters that the BP model has the highest stability. The WNN model as a whole is second to BP, and the test of the RBF model in the training set is the closest to the actual value, which is determined by the nature of the RBF model. For the RBF model, the closer the sample is to the data center, the more likely it is to be activated. The more it deviates from the training sample in the data center, the less the influence of the RBF method on it will be.

In order to directly observe the evaluation performance of the models, the comparison diagram of the measured value and the estimated value in the two sets of training set and testing set is drawn in Figure 2 of the WNN, BP, and RBF models. It can be seen from Figure 2a−d that the reference line of the WNN and BP model is very close to the least square line, but according to Figure 2e,f, the data points obtained by the BP model are closer to the reference line, that is, the simulated value is closer to the actual value. The training set data sets of the RBF model almost all fall on the reference line; the closer the data is to the data center, the more accurate is the prediction. For the prediction data with large deviation, values are far from the data center or do not fall within the width of the data center.

Figure 3 describes the distribution of the absolute error between the measured IFT and the estimated IFT. It can be seen from it that most of the error values of the BP model are distributed within 2%, and few of them are larger than 10%.

https://dx.doi.org/10.1021/acsomega.0c05290
ACS Omega 2021, 6, 4282−4288

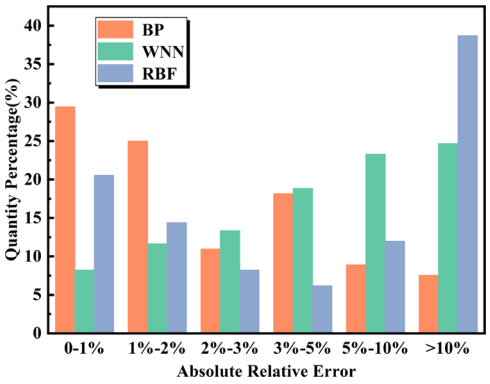

Figure 3. Error distribution diagram of CO_2−brine IFT of the models (i.e. BP, WNN, and RBF).

The error distribution of the WNN model is relatively average, and the RBF model error presents polarization distribution. The RBF performance is better than the WNN model in the range of low absolute error, but the performance is opposite in the range of high absolute error.

From the above analysis, it can be determined that the prediction ability of the WNN model is weaker than that of the BP model when the initial transfer vector is randomly selected. In order to further determine ability of the WNN model compared with the BP model, namely, to compare the difference between the two activation functions, the IFT comparison chart of the improved WNN (I_WNN) model is shown in Figure 4 after optimizing the WNN model of the initial transfer vector. The norms calculated are shown in Table 3. Compared with Table 2, it can be seen that the norms of the improved WNN model are still not as good as those obtained by the BP model. Therefore, from the essence of the two models, the performance of the sigmoid activation function is better than that of the wavelet basis function.

5.2. Influence of Variables. The IFT is determined by the relevant parameters. Because each parameter has a different impact on IFT, it is important to ensure the weight of each parameter. In this paper, the weight and threshold value of each layer calculated by the optimized WNN model is used to determine the correlation coefficient of each parameter, as shown in Figure 5 (the correlation coefficient of pressure is set as 1). It can be seen from the figure that pressure is the most important factor affecting IFT, followed by temperature; both

Table 3. Different Norms Computed to Assess the Improved WNN Model for Predicting CO_2−Brine IFT

	all	training set	testing set
MAE	2.0788	2.0592	2.1246
MARE	5.4612	5.4330	5.5272
MSE	7.3825	7.2286	7.7419
R^2	0.9560	0.9577	0.9516

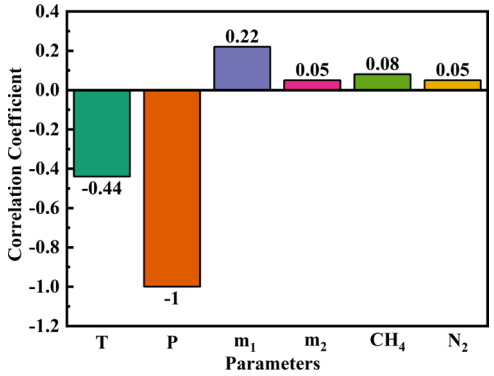

Figure 5. Correlation coefficient of the independent variables on the CO_2−brine IFT.

of them have a high proportion, and similar conclusions can be obtained in refs.[3,17,39] The reason for this result should be the phase change of the surrounding environment. Under the critical temperature and pressure of CO_2, CO_2 will remain liquid, but once it exceeds this value, it will become gaseous. At this time, a sudden change of IFT will occur. Figure 6 is drawn according to ref 15; it can be observed from Figure 6a that the slope of the IFT curve changes dramatically after nodes a, b, and c; as shown in Figure 6b, the change in IFT is also obvious when the temperature changes but not as much as the change in pressure. Therefore, in the process of the CO_2 brine IFT experiment, whether the temperature and pressure can be accurately controlled is the most important condition.

6. CONCLUSIONS

In order to estimate the IFT between impure CO_2 and brine a in a wide range of thermodynamic properties, 974 data sets from the literature are integrated carefully and divided into the training set (70%) and testing set (30%). The WNN, BP, RBF,

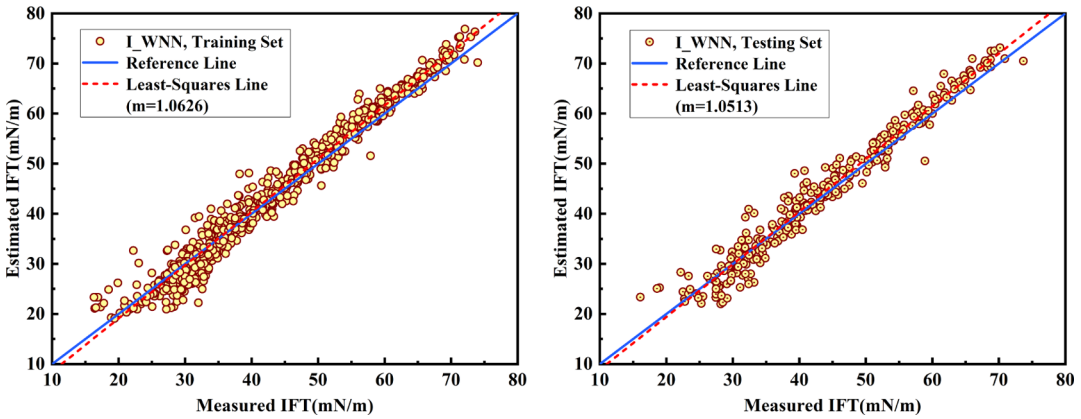

Figure 4. Comparison between the results obtained by the improved WNN model and the actual data of CO_2−brine IFT. (m is the slope of the least-squares line).

https://dx.doi.org/10.1021/acsomega.0c05290
ACS Omega 2021, 6, 4282−4288

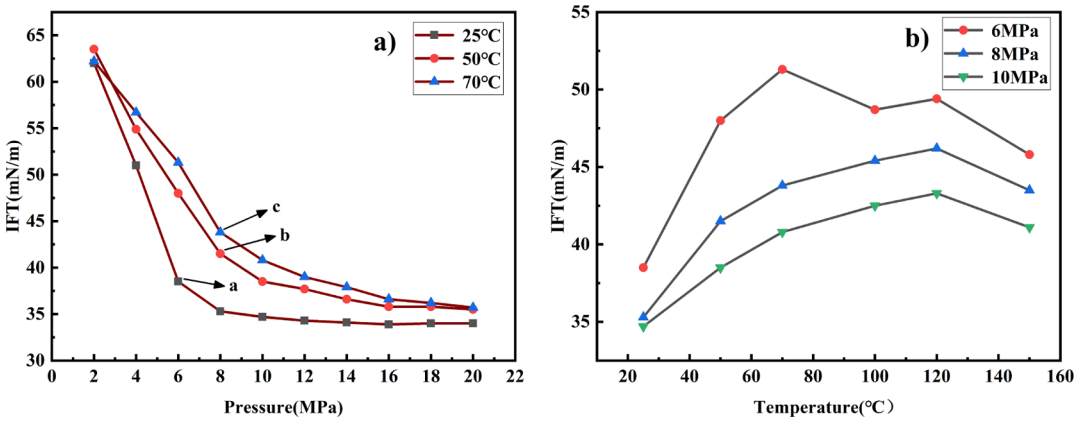

Figure 6. CO_2–brine IFT scatter plots of temperature and pressure.

and improved WNN model based on the ANN model are used to measure the performance of prediction of CO_2–brine IFT. The BP, RBF, and improved WNN models have their own advantages, which are suitable for different situations. The overall evaluation of the BP model is the best; the RBF model is suitable for large database models, and the I_WNN model is the most stable and reliable model, for which R^2 is above 0.95 in both the training set and testing set. As a general drawback of neural networks, the prediction performance is greatly influenced by the quality of samples and the initial transfer vector; the results of each run of the BP and RBF models will be different. The I_WNN model improves the prediction stability by improves the initial transfer vector. As the main parameters of IFT, pressure and temperature have great influence on the results of IFT. Therefore, the disturbance of the surrounding environment caused by the instability of these two parameters should be avoided in the process of the IFT experiment.

AUTHOR INFORMATION

Corresponding Author

Yu Liu – *Key Laboratory of Ocean Energy Utilization and Energy Conservation of the Ministry of Education, Dalian University of Technology, Dalian 116024, China;* orcid.org/0000-0002-6003-9121; Phone: +8613604083667; Email: liuyu@dlut.edu.cn

Authors

Xiaojie Liu – *Key Laboratory of Ocean Energy Utilization and Energy Conservation of the Ministry of Education, Dalian University of Technology, Dalian 116024, China;* orcid.org/0000-0002-1395-5653

Meiheriayi Mutailipu – *Key Laboratory of Ocean Energy Utilization and Energy Conservation of the Ministry of Education, Dalian University of Technology, Dalian 116024, China*

Jiafei Zhao – *Key Laboratory of Ocean Energy Utilization and Energy Conservation of the Ministry of Education, Dalian University of Technology, Dalian 116024, China;* orcid.org/0000-0001-8401-4204

Complete contact information is available at: https://pubs.acs.org/10.1021/acsomega.0c05290

Notes

The authors declare no competing financial interest.

ACKNOWLEDGMENTS

We are grateful to Prof. Frank Quina (Associate Editor, ACS Omega) and Dr. Natasa Medic (Peer Review Analyst, ACS Omega) for their assistance in preparing this editorial.

REFERENCES

(1) IEA. *Global Energy & CO_2 Status Report*, 2019. https://www.iea.org/reports/global-energy-co2-status-report-2019.

(2) Orr, F. M. Storage of Carbon Dioxide in Geologic Formations. *J. Pet. Technol.* **2004**, *56*, 90–97.

(3) Amooie, M. A.; Hemmati-Sarapardeh, A.; Karan, K.; Husein, M. M.; Soltanian, M. R.; Dabir, B. Data-driven modeling of interfacial tension in impure CO_2-brine systems with implications for geological carbon storage. *Int. J. Greenhouse Gas Control* **2019**, *90*, 102811.

(4) Zhang, J.; Feng, Q.; Wang, S.; Zhang, X.; Wang, S. Estimation of CO_2–brine interfacial tension using an artificial neural network. *J. Supercrit. Fluids* **2016**, *107*, 31–37.

(5) Aggelopoulos, C. A.; Robin, M.; Perfetti, E.; Vizika, O. CO_2/$CaCl_2$ solution interfacial tensions under CO_2 geological storage conditions: Influence of cation valence on interfacial tension. *Adv. Water Resour.* **2010**, *33*, 691–697.

(6) Aggelopoulos, C. A.; Robin, M.; Vizika, O. Interfacial tension between CO_2 and brine ($NaCl+CaCl_2$) at elevated pressures and temperatures: The additive effect of different salts. *Adv. Water Resour.* **2011**, *34*, 505–511.

(7) Arif, M.; Al-Yaseri, A. Z.; Barifcani, A.; Lebedev, M.; Iglauer, S. Impact of pressure and temperature on CO2-brine-mica contact angles and CO2-brine interfacial tension: Implications for carbon geo-sequestration. *J. Colloid Interface Sci.* **2016**, *462*, 208–215.

(8) Bachu, S.; Bennion, D. B. Interfacial Tension between CO_2, Freshwater, and Brine in the Range of Pressure from (2 to 27) MPa, Temperature from (20 to 125) °C, and Water Salinity from (0 to 334 000) $mg{\cdot}L^{-1}$. *J. Chem. Eng.* **2009**, *54*, 765–775.

(9) Bachu, S.; Brant Bennion, D. Dependence of CO_2 -brine interfacial tension on aquifer pressure, temperature and water salinity. *Energy Procedia* **2009**, *1*, 3157–3164.

(10) Bikkina, P. K.; Shoham, O.; Uppaluri, R. Equilibrated Interfacial Tension Data of the CO_2–Water System at High Pressures and Moderate Temperatures. *J. Chem. Eng. Data* **2011**, *56*, 3725–3733.

(11) Chalbaud, C.; Robin, M.; Lombard, J.-M.; Martin, F.; Egermann, P.; Bertin, H. Interfacial tension measurements and wettability evaluation for geological CO_2 storage. *Adv. Water Resour.* **2009**, *32*, 98–109.

(12) Chiquet, P.; Daridon, J.-L.; Broseta, D.; Thibeau, S. CO_2/water interfacial tensions under pressure and temperature conditions of CO_2 geological storage. *Energy Convers. Manage.* **2007**, *48*, 736–744.

(13) Georgiadis, A.; Maitland, G.; Trusler, J. P. M.; Bismarck, A. Interfacial Tension Measurements of the (H_2O + CO_2) System at

https://dx.doi.org/10.1021/acsomega.0c05290
ACS Omega 2021, 6, 4282–4288

Elevated Pressures and Temperatures. *J. Chem. Eng. Data* **2010**, *55*, 4168−4175.
(14) Hebach, A.; Oberhof, A.; Dahmen, N.; Kögel, A.; Ederer, H.; Dinjus, E. Interfacial Tension at Elevated Pressuress Measurements and Correlations in the Water + Carbon Dioxide System. *J. Chem. Eng.* **2002**, *47*, 1540−1546.
(15) Li, X.; Boek, E.; Maitland, G. C.; Trusler, J. P. M. Interfacial Tension of (Brines + CO_2): (0.864 NaCl + 0.136 KCl) at Temperatures between (298 and 448) K, Pressures between (2 and 50) MPa, and Total Molalities of (1 to 5) mol·kg^{-1}. *J. Chem. Eng.* **2012**, *57*, 1078−1088.
(16) Li, X.; Boek, E. S.; Maitland, G. C.; Trusler, J. P. M. Interfacial Tension of (Brines + CO_2): $CaCl_2$(aq), $MgCl_2$(aq), and Na_2SO_4(aq) at Temperatures between (343 and 423) K, Pressures between (2 and 50) MPa, and Molalities of (0.5 to 5) mol·kg^{-1}. *J. Chem. Eng. Data* **2012**, *57*, 1369−1375.
(17) Li, Z.; Wang, S.; Li, S.; Liu, W.; Li, B.; Lv, Q.-C. Accurate Determination of the CO_2−Brine Interfacial Tension Using Graphical Alternating Conditional Expectation. *Energy Fuels* **2014**, *28*, 624−635.
(18) Ren, Q.-Y.; Chen, G.-J.; Yan, W.; Guo, T.-M. Interfacial Tension of (CO_2+CH_4)+Water from 298K to 373K and Pressures up to 30 MPa. *J. Chem. Eng.* **2000**, *45*, 610−612.
(19) Yan, W.; Zhao, G.-Y.; Chen, G.-J.; Guo, T.-M. Interfacial Tension of (Methane + Nitrogen) + Water and (Carbon Dioxide + Nitrogen) + Water Systems. *J. Chem. Eng.* **2001**, *46*, 1544−1548.
(20) Biscay, F.; Ghoufi, A.; Lachet, V.; Malfreyt, P. Monte Carlo calculation of the methane-water interfacial tension at high pressures. *J. Chem. Phys.* **2009**, *131*, 124707.
(21) Iglauer, S.; Mathew, M. S.; Bresme, F. Molecular dynamics computations of brine-CO_2 interfacial tensions and brine-CO_2-quartz contact angles and their effects on structural and residual trapping mechanisms in carbon geo-sequestration. *J. Colloid Interface Sci.* **2012**, *386*, 405−414.
(22) Li, W.; Jin, Z. Molecular dynamics simulations of natural gas-water interfacial tensions over wide range of pressures. *Fuel* **2019**, *236*, 480−492.
(23) Li, W.; Jin, Z. Effect of ion concentration and multivalence on methane-brine interfacial tension and phenomena from molecular perspectives. *Fuel* **2019**, *254*, 115657.
(24) Míguez, J. M.; Garrido, J. M.; Blas, F. J.; Segura, H.; Mejía, A.; Piñeiro, M. M. Comprehensive Characterization of Interfacial Behavior for the Mixture CO_2+H_2O+CH_4: Comparison between Atomistic and Coarse Grained Molecular Simulation Models and Density Gradient Theory. *J. Phys. Chem. C* **2014**, *118*, 24504−24519.
(25) Miqueu, C.; Míguez, J. M.; Piñeiro, M. M.; Lafitte, T.; Mendiboure, B. Simultaneous application of the gradient theory and Monte Carlo molecular simulation for the investigation of methane/water interfacial properties. *J. Phys. Chem. B* **2011**, *115*, 9618−9625.
(26) Nielsen, L. C.; Bourg, I. C.; Sposito, G. Predicting CO_2−water interfacial tension under pressure and temperature conditions of geologic CO_2 storage. *Geochim. Cosmochim. Acta* **2012**, *81*, 28−38.
(27) Reed, S. K.; Westacott, R. E. The interface between water and a hydrophobic gas. *Phys. Chem. Chem. Phys.* **2008**, *10*, 4614−4622.
(28) Sakamaki, R.; Sum, A. K.; Narumi, T.; Ohmura, R.; Yasuoka, K. Thermodynamic properties of methane/water interface predicted by molecular dynamics simulations. *J. Chem. Phys.* **2011**, *134*, 144702.
(29) Silvestri, A.; Stipp, S. L. S.; Andersson, M. P. Predicting CO_2-H_2O Interfacial Tension Using COSMO-RS. *J. Chem. Theory Comput.* **2017**, *13*, 804−810.
(30) Tsuji, S.; Liang, Y.; Kunieda, M.; Takahashi, S.; Matsuoka, T. Molecular Dynamics Simulations of the CO_2-Water-silica Interfacial Systems. *Energy Procedia* **2013**, *37*, 5435−5442.
(31) Yang, Y.; Narayanan Nair, A. K.; Sun, S. Molecular Dynamics Simulation Study of Carbon Dioxide, Methane, and Their Mixture in the Presence of Brine. *J. Phys. Chem. B* **2017**, *121*, 9688−9698.
(32) Vasseghian, Y.; Bahadori, A.; Khataee, A.; Dragoi, E.-N.; Moradi, M. Modeling the Interfacial Tension of Water-Based Binary and Ternary Systems at High Pressures Using a Neuro-Evolutive Technique. *ACS Omega* **2019**, *5*, 781−790.
(33) Zhang, J.; Feng, Q.; Zhang, X.; Zhang, X.; Yuan, N.; Wen, S.; Wang, S.; Zhang, A. The use of an artificial neural network to estimate natural gas/water interfacial tension. *Fuel* **2015**, *157*, 28−36.
(34) Niroomand-Toomaj, E.; Etemadi, A.; Shokrollahi, A. Radial basis function modeling approach to prognosticate the interfacial tension CO_2/Aquifer Brine. *J. Mol. Liq.* **2017**, *238*, 540−544.
(35) Partovi, M.; Mosalanezhad, M.; Lotfi, S.; Barati-Harooni, A.; Najafi-Marghmaleki, A.; Mohammadi, A. H. On the estimation of CO_2-brine interfacial tension. *J. Mol. Liq.* **2017**, *243*, 265−272.
(36) Chen, Z.; Yang, D. Prediction of Equilibrium Interfacial Tension between CO_2 and Water Based on Mutual Solubility. *Ind. Eng. Chem. Res.* **2018**, *57*, 8740−8749.
(37) Liu, Q.; Sun, P.; Fu, X.; Zhang, J.; Yang, H.; Gao, H.; Li, Y. Comparative analysis of BP neural network and RBF neural network in seismic performance evaluation of pier columns. *Mech. Syst. Signal Process.* **2020**, *141*, 106707.
(38) Khayamian, T.; Esteki, M. Prediction of solubility for polycyclic aromatic hydrocarbons in supercritical carbon dioxide using wavelet neural networks in quantitative structure property relationship. *J. Supercrit. Fluids* **2004**, *32*, 73−78.
(39) Dehaghani, A. H. S.; Soleimani, R. On the Estimation of Interfacial Tension for Geological CO_2 Storage. *Chem. Eng. Technol.* **2019**, *42*, 680−689.

https://dx.doi.org/10.1021/acsomega.0c05290
ACS Omega 2021, 6, 4282−4288